Structure
Article

Structure of an IgNAR-AMA1 Complex: Targeting a Conserved Hydrophobic Cleft Broadens Malarial Strain Recognition

Kylie A. Henderson,[1,2,3] Victor A. Streltsov,[1] Andrew M. Coley,[2,3] Olan Dolezal,[1] Peter J. Hudson,[1] Adrian H. Batchelor,[4] Aditi Gupta,[4] Tao Bai,[4] Vincent J. Murphy,[3] Robin F. Anders,[3] Michael Foley,[2,3,*] and Stewart D. Nuttall[1,*]

[1]CSIRO Molecular and Health Technologies, 343 Royal Parade, Parkville 3052, Australia
[2]Cooperative Research Centre for Diagnostics, GPO Box 2434, Brisbane 4001, Australia
[3]Biochemistry Department, La Trobe University, Bundoora 3086, Australia
[4]University of Maryland School of Pharmacy, Baltimore, MD 21201, USA
*Correspondence: m.foley@latrobe.edu.au (M.F.), stewart.nuttall@csiro.au (S.D.N.)
DOI 10.1016/j.str.2007.09.011

SUMMARY

Apical membrane antigen 1 (AMA1) is essential for invasion of erythrocytes and hepatocytes by *Plasmodium* parasites and is a leading malarial vaccine candidate. Although conventional antibodies to AMA1 can prevent such invasion, extensive polymorphisms within surface-exposed loops may limit the ability of these AMA1-induced antibodies to protect against all parasite genotypes. Using an AMA1-specific IgNAR single-variable-domain antibody, we performed targeted mutagenesis and selection against AMA1 from three *P. falciparum* strains. We present cocrystal structures of two antibody-AMA1 complexes which reveal extended IgNAR CDR3 loops penetrating deep into a hydrophobic cleft on the antigen surface and contacting residues conserved across parasite species. Comparison of a series of affinity-enhancing mutations allowed dissection of their relative contributions to binding kinetics and correlation with inhibition of erythrocyte invasion. These findings provide insights into mechanisms of single-domain antibody binding, and may enable design of reagents targeting otherwise cryptic epitopes in pathogen antigens.

INTRODUCTION

Malaria is a devastating parasitic infection that threatens approximately 40% of the world's population (WHO/UNICEF, 2005). *Plasmodium falciparum*, the most virulent malaria parasite infecting humans, has developed resistance to many of the drugs used for prophylaxis or therapy, and the development of a vaccine or novel therapeutic agent would represent a major advance toward controlling this devastating parasitic infection. A particularly promising vaccine candidate and potential drug target is apical membrane antigen 1 (AMA1) (Peterson et al., 1989). AMA1 is a type 1 integral membrane protein which is released from the micronemes onto the merozoite surface (Alexander et al., 2006; Healer et al., 2002; Narum and Thomas, 1994) and is located at the moving junction between the invading merozoite and erythrocyte membrane. Here, in complex with the rhoptry neck protein PfRON4 (Alexander et al., 2006), it plays a critical role in host cell invasion. AMA1 appears essential for parasite viability, and orthologs are conserved across other apicomplexan parasites (Hehl et al., 2000; Zhou et al., 2006).

Structurally, the AMA1 ectodomain consists of three domains (I, II, III) which when correctly folded, induce antibodies that inhibit merozoite invasion of host erythrocytes (Hodder et al., 2001; Kennedy et al., 2002). Whereas some inhibitory antibodies block proteolytic processing of AMA1 (Dutta et al., 2005), it is likely that steric inhibition of interaction with a ligand also mediates inhibition. Because of the extensive polymorphisms in AMA1 within *Plasmodium* species (Cheng and Saul, 1994; Cortes et al., 2003; Marshall et al., 1996), inhibition of merozoite invasion by anti-AMA1 antibodies exhibits considerable strain specificity (Hodder et al., 2001; Kennedy et al., 2002). The importance of AMA1 as a target of naturally acquired protective immune responses is not clear, but the selection pressure exerted by host immune responses has been responsible for at least some of the polymorphisms in AMA1 (Polley et al., 2003). Many of these polymorphic residues are located on flexible loops in domain I, which are recognized by naturally occurring antibody responses.

The recent solution of the first crystallographic structures of domains I–III of *P. vivax* AMA1 (Pizarro et al., 2005) and domains I and II of *P. falciparum* strain 3D7 AMA1 (Bai et al., 2005) revealed that the flexible loops surround an extended cleft or trough which is hypothesized to be a ligand-binding site. The base of the cleft is rich in solvent-exposed hydrophobic side chains, several of which are well conserved across diverse AMA1 proteins. For example, residue Tyr251 rises above the surface at the center of the cleft and is conserved in *Plasmodium* species and

the related *Toxoplasma gondii* and *Babesia bovis* parasites (Hehl et al., 2000). Conversely, most of the loops that surround the cleft are polymorphic in *P. falciparum* and related species (Bai et al., 2005). These flexible and diverse loops may facilitate evasion of otherwise protective antibody responses and also protect a conserved site(s) critical for AMA1 function. This concept has precedence in other important human pathogens, such as the polymorphisms that surround the sialic acid binding pocket of influenza neuraminidase (Varghese et al., 1998) and the conformational masking of HIV gp120 from antibodies (Kwong et al., 2002). Importantly, development of reagents targeting these two epitopes has depended, respectively, upon (1) sophisticated structure-based drug design resulting in the anti-influenza therapeutic Relenza (Varghese, 1999) and (2) isolation of an unusual human antibody from an HIV patient that recognizes gp120 through heavy-chain-only residues (Zhou et al., 2007). Thus, if the hypothesis that AMA1 has evolved to avoid and misdirect the human immune response is true, then effective targeting of cross-strain AMA1 variants may well rely on nonconventional or novel designed molecules.

Fortunately, the recombinant antibody armory now includes such proteins (Holliger and Hudson, 2005). For example, single-domain antibodies represent a distinct subclass of immune receptors where antigen binding is encapsulated within a *single* immunoglobulin domain of between 13 and 15 kDa in size (Nuttall et al., 2000). Naturally occurring examples are the immunoglobulin new antigen receptors (IgNARs) from sharks (Greenberg et al., 1993) and the V_HH isotype from camels and llamas (Hamers-Casterman et al., 1993), both of which are heavy-chain homodimers with no associated light chains. Although these isotypes have followed distinct evolutionary pathways separated by hundreds of millions of years, they display strikingly similar three-dimensional architectures, including large CDR3 loop regions which provide extensive variability and surface area to compensate for the absence of light-chain hypervariable regions (Nguyen et al., 2002; Roux et al., 1998; Streltsov et al., 2004). IgNAR variable domains (V_{NAR}s; as distinct from V_H, V_L, and V_HH domains) are also extremely stable, refolding without significant loss of function after treatment under a variety of denaturing conditions (Liu et al., 2007).

Structural studies aimed at dissecting the precise nature of the V_{NAR}-antigen interaction reveal that the true antibody paratope consists of the CDR3 and CDR1 loops with contributions from the adjacent heavy loop 4 (Stanfield et al., 2004; Streltsov et al., 2004). There is little input from the CDR2 region, which is severely truncated and wraps around the lower half of the Ig framework in a manner reminiscent of I set immunoglobulins (Streltsov and Nuttall, 2005). Cocrystallographic structures of V_{NAR} domains in complex with lysozyme show the dominant and extended CDR3 loops accessing the lysozyme active site cleft, an epitope not normally recognized by murine monoclonal antibodies, which preferentially target the hydrophobic faces of the antigen (Stanfield et al., 2007). This apparent preference for cleft-like structures is supported by a growing collection of crystallographic structures for camelid V_HH-antigen pairs, although in these instances a more diverse range of CDR3 conformations has been observed (De Genst et al., 2006).

Single-domain antibody reagents can be readily produced as recombinant proteins in heterologous systems such as *Escherichia coli*, and generated as immune repertoires displayed on the surface of bacteriophages (phage display) or completely translated in vitro (ribosome display). We and others have used this approach to generate shark molecular libraries based on both type 1 and type 2 V_{NAR}s, which are distinguished by their patterns of loop-stabilizing disulfide bond linkages (type 1, CDR3-framework; type 2, CDR1–CDR3) (Dooley et al., 2003; Nuttall et al., 2001; Simmons et al., 2007). Previously, we utilized such libraries to isolate a low-affinity type 2 V_{NAR} domain, designated 12Y-2, which targeted *P. falciparum* strain 3D7 AMA1 with 300 nM affinity. Atypically, this V_{NAR} showed no interloop disulfide bonds, and mutations generated by random mutagenesis improved binding by up to 10-fold and mapped to the laterally extended CDR3 loop region (Nuttall et al., 2004). In order to explore the hypothesis that single-domain antibodies can target otherwise cryptic epitopes, we have now designed molecular libraries based on the original 12Y-2 V_{NAR} and selected for variants with improved binding to different AMA1s. We report here one such family of V_{NAR}s, and describe two V_{NAR}-AMA1 cocrystallographic structures. Our results allow us to better understand the mechanisms of single-domain antibody cleft targeting and antigen recognition, and suggest possible strategies for targeting of conserved apicomplexan parasite epitopes.

RESULTS

A V_{NAR} Library Targeting AMA1

The parental 12Y-2 V_{NAR} has ~300 nM affinity for *P. falciparum* AMA1 of the 3D7 strain, but does not bind strain W2mef or HB3 AMA1s. Individual single-residue mutations at positions Pro90 and Phe100 in the extended CDR3 loop structure enhanced this binding affinity for AMA1 3D7 by up to 10-fold, but did not yield broader strain specificity (Nuttall et al., 2004). To further explore variability within the extended CDR3 loop structure, we targeted the ten residues at the loop tip (Leu89–Leu98 inclusive) which dominate the proposed paratope (Figure 1A). A series of libraries were designed which varied in length, sequence, and coding strategies for this region. The randomization strategy included biases toward aromatic residues traditionally overrepresented in antigen-binding loops (Collis et al., 2003) and a bias toward hydrophobic residues at position 98 (Figure 1B). Library construction utilized a series of degenerative oligonucleotide primers (see Table S1 in the Supplemental Data available with this article online) and resulted in a final library size of $>5 \times 10^7$ independent clones, exhibiting extensive diversity in loop length and amino acid sequence.

This bacteriophage-displayed library was sequentially panned against the HB3, W2mef, HB3, and 3D7 forms of

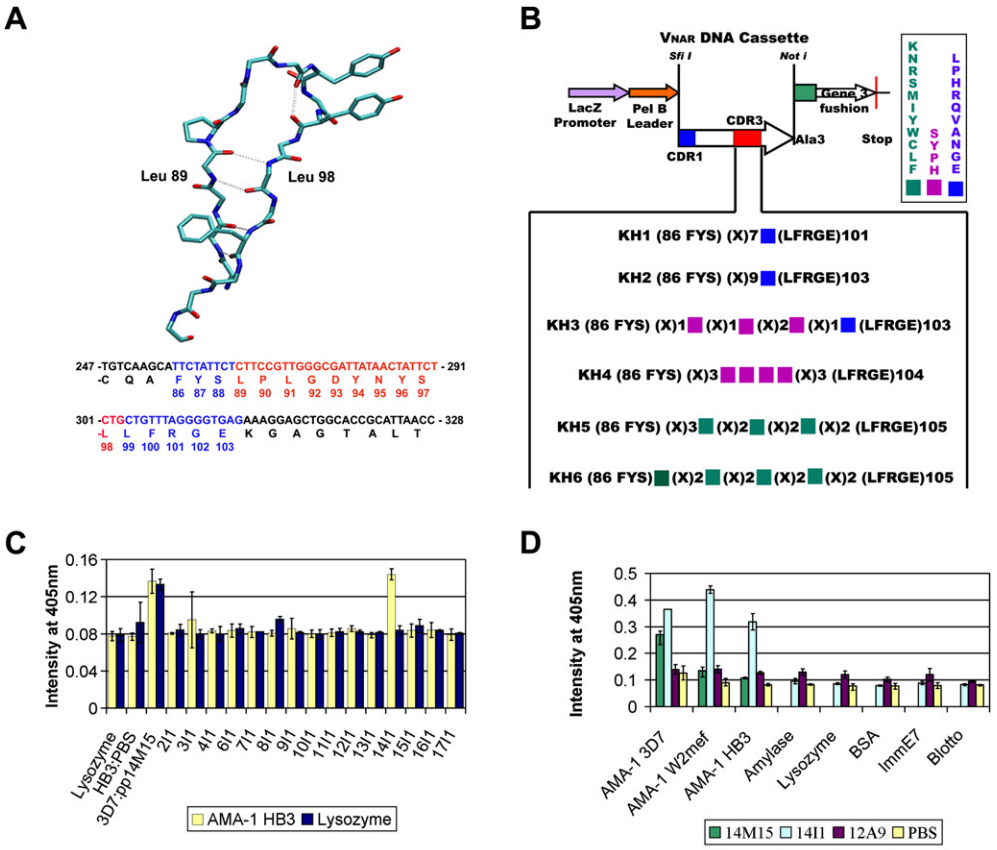

E

```
12Y2          1  AWVDQTPRTATKETGESLTINCVLRDASFELKDTGWYRTKLGSTNEQSISIGGRYVE
14M8          1  AWVDQTPRTATKETGESLTINCVLRDTSFELKDTGWYRTKLGSTNEQSISIGGRYVE
14M15         1  AWVDQTPRTATKETGESLTINCVLRDASFELKDTGWYRTKLGSTNEQSISIGGRYVE
14I1          1  AWVDQTPRTATKETGESLTINCVLRDASLELKDTGWYRTKLGSTNEQSISIGGRYVE
14I1-Y2       1  AWVDQTPRTATKETGESLTINCVLRDASFELKDTGWYRTKLGSTNEQSISIGGRYVE
14I1-M15      1  AWVDQTPRTATKETGESLTINCVLRDASFELKDTGWYRTKLGSTNEQSISIGGRYVE
14I1-M8       1  AWVDQTPRTATKETGESLTINCVLRDASFELKDTGWYRTKLGSTNEQSISIGGRYVE

12Y2         58  TVNKGSKSFSLRISDLRVEDSGTYKCQAFYSLPLGDYNYSLLFRGEKGAGTALTVK
14M8         58  TVNKGSKSFSLRISDLRVEDSGTYKCQAFYSLPLGDYNYSLLLRGEKGAGTALTVK
14M15        58  TVNKGSKSFSLRISDLRVEDSGTYKCQAFYSLLLGDYNYSLLFRGEKGAGTALTVK
14I1         58  TVNKGSKSFSLRISDLRVEDSGTYKCQAFYSLPLRDYNYSLLFRGEKGAGTALTVK
14I1-Y2      58  TVNKGSKSFSLRISDLRVEDSGTYKCQAFYSLPLRDYNYSLLFRGEKGAGTALTVK
14I1-M15     58  TVNKGSKSFSLRISDLRVEDSGTYKCQAFYSLLLRDYNYSLLFRGEKGAGTALTVK
14I1-M8      58  TVNKGSKSFSLRISDLRVEDSGTYKCQAFYSLPLRDYNYSLLLRGEKGAGTALTVK
```

Figure 1. V_{NAR} Library Design

(A) Structure of the 12Y-2 V_{NAR} elongated CDR3. Residues Leu89–Leu98 targeted for randomization during library construction (red) form a significant portion of the dominant CDR3 loop region (blue).

(B) Six degenerate oligonucleotide primers (KH1–KH6) were designed to yield divergent randomization patterns. Variability was introduced through loop length variability (8–12 residues) and by incorporation of coding bias toward hydrophobic residues (blue boxes), aromatic ring structures (pink and green boxes), or random residues (X). Libraries were cloned as cassettes into the pFab5c.His phagemid display vector.

(C) ELISA of *E. coli* periplasmic fractions assayed for binding to immobilized *P. falciparum* HB3 antigen. Clone 14I-1 shows significant binding above background and lysozyme negative control antigen. Data are represented as the mean ± standard error of duplicate experiments.

(D) ELISA testing of affinity-purified V_{NAR} proteins (14I-1, 14M-15, 12A-9) for cross-strain AMA1 binding. Data are represented as the mean ± standard error of triplicate experiments.

(E) V_{NAR} variants illustrating combinations of single affinity-enhancing mutations (black) within CDR1 and CDR3 regions (gray).

AMA1. These four rounds of panning were sufficient for positive enrichment as indicated by rising phage titers (data not shown), whereupon V_{NAR} DNA cassettes were rescued and subcloned into the periplasmic expression vector pGC, and multiple *E. coli* periplasmic fractions screened for binding. One particularly promising clone, designated 14I-1, showed enhanced binding to AMA1 HB3 (Figure 1C), and testing of FLAG tag affinity-purified protein showed significant binding to all three forms of AMA1 but not negative control antigens (Figure 1D). DNA sequencing revealed two mutations: (1) Phe29Leu, a previously characterized CDR1 mutant (Kopsidas et al., 2006) derived from variability within the DNA templates used in library construction and (2) Gly92Arg, a novel CDR3 mutant. As a first step to dissecting the relative contribution of these changes to antigen binding, a series of seven variant clones incorporating combinations of previously validated affinity-enhancing mutations 14M-15 (Pro90Leu) and 14M-8 (Phe100Leu) was produced (Figure 1E). For consistency, position 29 was additionally back-mutated to phenylalanine. This set of V_{NAR} proteins was simultaneously expressed in *E. coli* and affinity purified. No significant differences were observed between the variants in terms of purification yields or by standard protein chemistry techniques such as size-exclusion chromatography, except as detailed below (Figure S1, and data not shown).

V_{NAR} AMA1 Binding Kinetics Correlate with Inhibition of Erythrocyte Invasion

Data on the binding kinetics of all seven V_{NAR} proteins to the three forms of AMA1 were obtained by Biacore biosensor analysis (Table 1; Figure S2). From this comprehensive data set, the key findings were as follows. (1) The parental V_{NAR}s 12Y-2, 14M-15, and 14M-8 bind AMA1 3D7 but not strains W2mef or HB3, confirming previous findings. (2) V_{NAR} 14I-1 showed ~5 nM binding to AMA1 3D7, which is a 6-fold increase in affinity over previous variants. The dominant mutation appears to be Gly92Arg, as combination with variant Pro90Leu was not additive at the kinetic level. (3) The mutation Phe100Leu, in combination with Gly92Arg, produced markedly reduced binding compared to the two individual variants, confirming our previous observations that modification of position 100 abrogates Phe29-Phe100-Tyr87 aromatic ring interactions when combined with other CDR mutations. Such residue combinations appear to adversely affect the V_{NAR} tertiary structure, resulting in lowered protein expression levels, aberrant gel-filtration profiles, and reduced binding (Kopsidas et al., 2006) (data not shown). (4) Mutation Gly92Arg results in moderate binding to AMA1 W2mef (~140 nM) and low-affinity binding to AMA1 HB3 (~700 nM). (5) There are significant kinetic differences between the interactions of 14I1-Y2 with W2mef and HB3, and 14I1-M15 with W2mef and HB3, suggesting, notwithstanding point 2 above, that mutation Pro90Leu contributes to enhanced cross-strain binding even in the presence of the mutation Gly92Arg.

Dissection of the relative contributions to binding of the association (K_A) and dissociation (K_D) rates suggests that the differences in binding affinities are mostly attributable to slower dissociation rates (Table 1). For example, the dissociation constants are notably different (12Y-2 V_{NAR} dissociates fastest, ~5 times faster than the 14M-8 and 14M-15 V_{NAR}s and 20–30 times faster than 14I-1 for AMA1 3D7). In contrast, the association rates of V_{NAR}s 14M-8, 14M-15, 14I-1, 14I1-Y2, and 14I1-M15 fall within a narrow range of 8.32×10^4 to 1.27×10^5. However, because of overlapping standard errors for the triplicate set of experiments with 14I-1 and 14I1-M15, we are unable to definitively state whether there is a significant difference in the association rate for these two proteins.

The ability of anti-AMA1 reagents to inhibit *P. falciparum* invasion of erythrocytes in in vitro culture is an important measure of functionality and a means of identifying critical epitopes (Basco et al., 1995; Coley et al., 2006). Thus, a series of growth inhibition assays were performed for the panel of recombinant V_{NAR}s against parasite strains 3D7, W2mef, and HB3, mirroring the Biacore kinetic studies (Figures 2A and 2B, and data not shown). The V_{NAR}s 14M-15, 14M-8, 14I-1, 14I1-Y2, and 14I1-M15 potently inhibited invasion of 3D7 parasites; in contrast, minimal inhibition was observed for 12Y-2, 14I1-M8, and the nonbinding V_{NAR} 12A-9 (Table 2). V_{NAR}s 14I-1 and 14I1-M15 successfully inhibited AMA1 W2mef at high protein concentrations, but no inhibition of HB3 parasites was observed (Table 2, and data not shown). Slight variations were observed for the relative inhibitory (IC_{50}) values between different series of experiments, consistent with the variability inherent within biological assays, but a clear trend was apparent in the ranking of the V_{NAR} variants. 14I1-M15 (IC_{50} ~15 μg/ml) was consistently the most potent inhibitor, followed by 14M-8/14M-15/14I-1/14I1-Y2. This provided further evidence that position 90 and 92 mutations are additive despite the kinetic data for AMA1 3D7 binding. No invasion inhibition was observed where affinities (as determined by Biacore) exceeded K_D ~600 nM (Tables 1 and 2), suggesting that a threshold exists at ~600 nM above which the antibody is unable to effectively inhibit/compete for binding with the as yet uncharacterized natural ligand for AMA1.

Structures of the V_{NAR}-AMA1 Complex

We crystallized domains I and II of AMA1 3D7 (residues N104–E438) (Gupta et al., 2005) in complex with both V_{NAR}s 14I-1 and 14I1-M15. The crystallographic structures were refined to a similar R factor of ~20% (resolution 2.35 and 2.45 Å, respectively) and are almost identical for both V_{NAR} (root-mean-square deviation [rmsd] of 0.278/0.350 Å for 114/116 residues) and AMA1 (rmsd of 0.379/0.405 Å for 314/319 residues) molecules. Details of crystallization and structure determination are provided in Experimental Procedures, and statistics for X-ray data collection and structure determination are summarized in Table 3.

The overall structures reveal the V_{NAR} CDR3 loop adopting an extended conformation and penetrating laterally into an elongated hydrophobic cleft on the AMA1 surface (Figure 3A). By targeting this cleft region, the V_{NAR}

Table 1. V_{NAR} Binding Kinetics for Three Different Recombinant AMA1 Strain Variants

		AMA1 3D7			AMA1 W2mef			AMA1 HB3		
V_{NAR}	Mutation	Binding Affinity K_D(nm)	On-Rate: Association Constant(1/ms)	Off-Rate: Dissociation Constant(1/s)	Binding Affinity K_D(nm)	On-Rate: Association Constant(1/ms)	Off-Rate: Dissociation Constant(1/s)	Binding Affinity K_D(nm)	On-Rate: Association Constant(1/ms)	Off-Rate: Dissociation Constant(1/s)
12Y-2	None	708 ± 357	$2.38 \times 10^4 \pm 1.22 \times 10^4$	$1.32 \times 10^{-2} \pm 1.94 \times 10^{-3}$	No binding[a]	No binding[a]	No binding[a]	No binding	No binding	No binding
14M-15	CDR3 Pro90Leu	31 ± 6.8	$8.80 \times 10^4 \pm 8.74 \times 10^3$	$2.76 \times 10^{-3} \pm 7.33 \times 10^{-4}$	No binding	No binding	No binding	No binding[a]	No binding[a]	No binding[a]
14M-8	CDR1 Ala27Thr CDR3 Phe100Leu	31 ± 2.2	$8.32 \times 10^4 \pm 4.03 \times 10^3$	$2.57 \times 10^{-3} \pm 1.15 \times 10^{-4}$	No binding[a]	No binding[a]	No binding[a]	No binding	No binding	No binding
14I-1	CDR1 Phe29Leu CDR3 Gly92Arg	4.8 ± 2.2	$8.37 \times 10^4 \pm 1.05 \times 10^4$	$4.12 \times 10^{-4} \pm 1.65 \times 10^{-4}$	141 ± 13	$3.73 \times 10^4 \pm 2.40 \times 10^3$	$5.25 \times 10^{-3} \pm 2.75 \times 10^{-4}$	717 ± 44	$2.29 \times 10^4 \pm 1.14 \times 10^2$	$1.64 \times 10^{-2} \pm 1.05 \times 10^{-3}$
14I1-Y2	CDR3 Gly92Arg	6.4 ± 1.6	$1.15 \times 10^5 \pm 2.26 \times 10^4$	$7.43 \times 10^{-4} \pm 1.56 \times 10^{-4}$	690 ± 46	$1.18 \times 10^4 \pm 2.45 \times 10^3$	$8.13 \times 10^{-3} \pm 1.17 \times 10^{-3}$	1808 ± 41	$8.84 \times 10^3 \pm 2.57 \times 10^3$	$1.60 \times 10^{-2} \pm 4.71 \times 10^{-3}$
14I1-M15	CDR3 Pro90Leu Gly92Arg	4.7 ± 2.0	$1.27 \times 10^5 \pm 5.23 \times 10^4$	$6.37 \times 10^{-4} \pm 6.65 \times 10^{-5}$	278 ± 8	$2.91 \times 10^4 \pm 2.05 \times 10^3$	$8.11 \times 10^{-3} \pm 6.55 \times 10^{-4}$	832 ± 174	$2.19 \times 10^4 \pm 1.97 \times 10^3$	$1.81 \times 10^{-4} \pm 3.62 \times 10^{-3}$
14I1-M8	CDR3 Gly92Arg Phe100Leu	570 ± 226	$9.47 \times 10^3 \pm 1.78 \times 10^3$	$2.78 \times 10^{-3} \pm 2.12 \times 10^{-4}$	No binding	No binding	No binding	No binding[a]	No binding[a]	No binding[a]
12A-9	None	No binding	No binding	No binding	No binding	No binding	No binding	No binding	No binding	No binding

[a] Inconsistent/low-level binding.

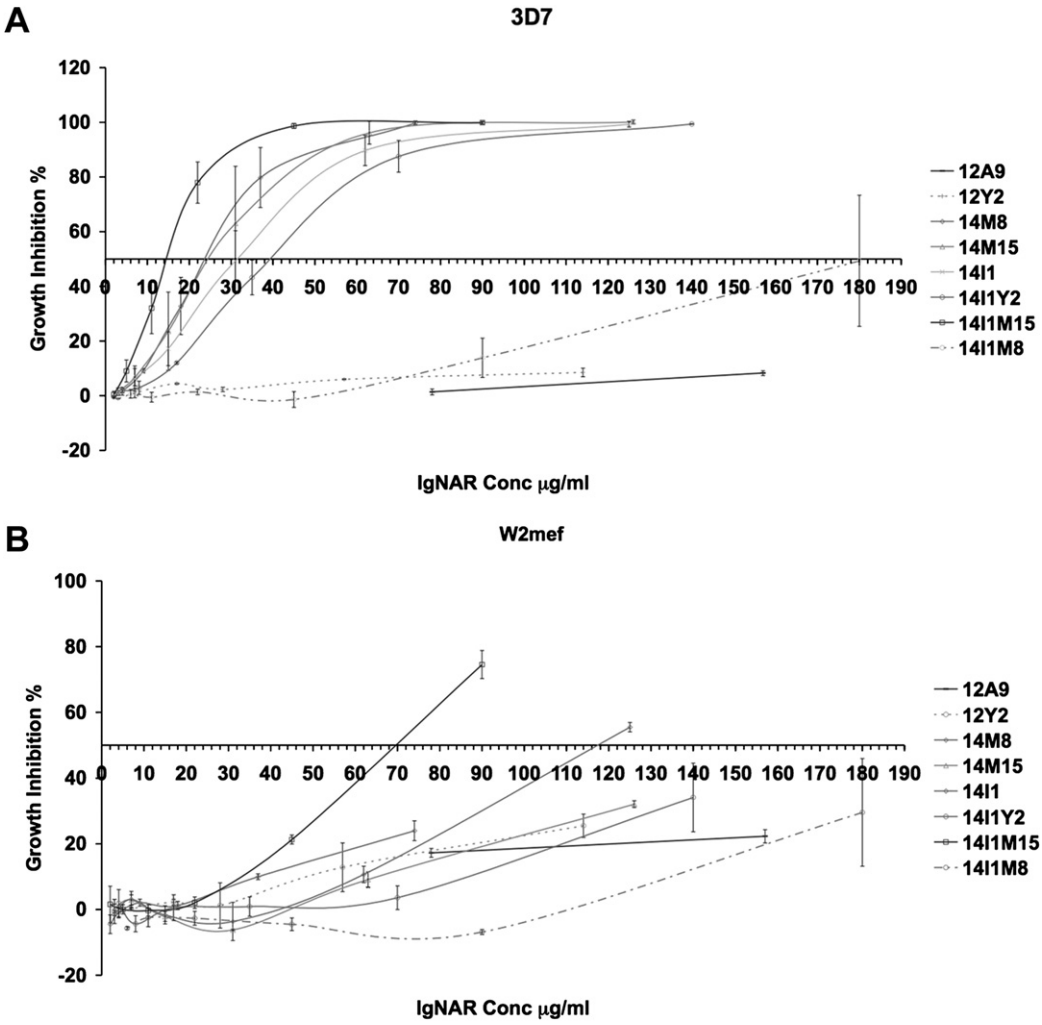

Figure 2. Parasite Invasion Inhibition

(A) Recombinant V_{NAR} domains inhibit invasion of erythrocytes by *P. falciparum* 3D7 parasites. Data are represented as the mean ± standard error of quadruplicate experiments.

(B) As for (A) except for *P. falciparum* W2mef parasites.

bypasses a large proportion of the highly variable polymorphic loop regions present on the previously described surface-exposed face of the AMA1 molecule (Figures 3B and 3C) (Bai et al., 2005). The molecular surface areas buried by the V_{NAR}-AMA1 complexes are extensive: 1205 Å^2 for 14I-1 and 1237 Å^2 for 14I1-M15. These figures compared favorably with complexes observed in other antibody-antigen interactions; however, many of these studies used differing programs, probe radii, and input parameters. Thus, in order to ensure consistency, we recalculated buried surfaces using the same program and probe parameters for a representative set of IgNAR and V_HH single-domain antibodies, and conventional antibodies targeting either AMA1 or cleft-like structures (Table S2). These figures confirmed our hypothesis that the V_{NAR}-AMA1 interface is one of the most extensive reported, comparable with representative single-domain and conventional antibodies derived from immunization of experimental animals. For example, the V_{NAR}s PBLA8 (799 Å^2) and HEL-5A7 (897 Å^2), and V_HHs cAbLys3 (908 Å^2) and AMD9 (1025 Å^2), were raised in sharks and camelids, respectively, and target the active site clefts of either lysozyme or α-amylase through extended CDR regions (Table S2). Interestingly, the buried surface area for the monoclonal inhibitory antibody 1F9, which also targets *P. falciparum* 3D7 (Coley et al., 2007), similarly buries an unusually large area on the AMA1 surface (1312 Å^2). The epitopes for this conventional murine antibody and the V_{NAR}s described here overlap to a considerable degree (Figure 3D). The shape complementarity values (Lawrence and Colman, 1993) of Sc = 0.71/0.66 for the V_{NAR}-AMA1 14I-1/14I1-14M15 complexes are also well within the accepted range for antibody-protein antigen interfaces.

Table 2. Relative IC_{50} and IC_{30} Values for V_{NAR} Inhibition of Parasite Erythrocyte Invasion

		AMA1 3D7		AMA1 W2mef	
V_{NAR}	Mutation	IC_{50}	IC_{30}	IC_{50}	IC_{30}
12Y-2	None	—	—	—	—
14M-15	CDR3 Pro90Leu	22 μg/ml	18 μg/ml	—	120 μg/ml
14M-8	CDR1 Ala27Thr; CDR3 Phe100Leu	22 μg/ml	18 μg/ml	—	90 μg/ml
14I-1	CDR1 Phe29Leu; CDR3 Gly92Arg	32 μg/ml	22 μg/ml	118 μg/ml	90 μg/ml
14I1-Y2	CDR3 Gly92Arg	40 μg/ml	28 μg/ml	—	130 μg/ml
14I1-M15	CDR3 Pro90Leu; CDR3 Gly92Arg	14 μg/ml	10 μg/ml	70 μg/ml	52 μg/ml
14I1-M8	CDR3 Gly92Arg; CDR3 Phe100Leu	~180 μg/ml	~130 μg/ml	—	~180 μg/ml
12A-9	None	Noninhibitory	Noninhibitory	Noninhibitory	Noninhibitory

V_{NAR} Conformational Changes upon Antigen Binding

The 14I-1 and 14I1-M15 CDR3 and CDR1 region electron densities were sufficiently well defined (Figures 4A and 4B, and data not shown) to allow comparison with the uncomplexed 12Y-2 V_{NAR} structure (Protein Data Bank [PDB] ID code: 1VES). Significant differences were observed for the three CDR3 loop regions (Figure 4C). The Gly92Arg mutation resulted in a laterally extended loop conformation in both complexed crystallographic forms. As the original glycine residue at this position allows significant conformational freedom, it is unlikely that these differences result from enhanced loop flexibility; rather, we suggest that the arginine side chain moves laterally upon binding to AMA1. Addition of Pro90Leu may then allow slightly enhanced loop conformational freedom (Figure 4C, compare red and blue traces) sufficient to provide superior cross-strain AMA1 interactions. Most significant were the variations observed in the position of aromatic residues Tyr94 and Tyr96. In the uncomplexed form, these residues point away from the backbone and against each other in an aromatic (phenyl) stacking interaction. When complexed with AMA1 in the AMA1/14I-1 structure, they now contact a network of AMA1 residues (see below) and adopt a perpendicular T stacking interaction (3.3 Å) relative to each other (Figure 4C). The distribution of electron density (Figure 4B, and data not shown) for these residues in the AMA1/14I1-M15 structure suggests that Tyr94 flips between an outward-facing orientation directed away from the antigen (as shown in Figure 4C) and alternatively occupancy of a hydrophobic pocket in the AMA1 hydrophobic cleft, similar to that observed for the AMA1/14I-1 structure. This is reflected in the B factors for residues Asp93-Tyr94-Asn95 in the 14I1-M15 structure (62.9 compared to 54.9 for the rest of the molecule). Comparison of the overlaid CDR1 loops for all three structures indicated minimal backbone displacement upon antigen binding (rmsd 12Y-2/14I-1: 1.493 Å; 12Y-2/14I1-M15: 1.373 Å), with only slight variations in side-chain orientation, most particularly at positions Phe/Leu29 and Lys32 (Figure 4D). The CDR2 in IgNAR antibodies is vestigial, and in this instance does not contact the AMA1 antigen.

Although these results suggest a possible example of "induced fit" upon antigen binding, definitive evidence supporting this hypothesis will, however, require future determination of the uncomplexed forms of both 14I-1 and 14I1-M15. In the only other structural analysis of free and complexed IgNAR antibodies (Stanfield et al., 2007), marked conformational distortion was also

Table 3. Data Collection, Structure Determination, and Refinement Statistics

Crystal	AMA1/14I-1	AMA1/14I1-M15
Diffraction Data		
Beamline	PF BL17A	PF BL17A
Space group	$P3_1$	$P3_1$
Unit cell dimensions (Å)	76.33, 140.39	76.48, 140.98
Resolution range (Å)	66.08–2.35 (2.41–2.35)	66.23–2.45 (2.51–2.45)
Wavelength (Å)	1.0000	0.96426
Unique reflections	34,389	28,622
Redundancy	5.4 (5.2)	5.0 (2.1)
Data completeness (%)	100 (100)	94 (65)
$I/\sigma(I)$	14.4 (1.0)	14.4 (1.6)
R_{merge} (%)[a]	0.10 (0.75)[a]	0.13 (0.57)[a]
Refinement		
R_{work} (%)[b]	20.1 (28.6)	18.9 (24.7)
R_{free} (%)[c]	28.4 (40.3)	28.2 (37.1)
Rms deviations		
Bond length (Å)	0.014	0.011
Bond angle (°)	1.584	1.340

Values in parentheses are for the highest shell.
[a] $R_{merge} = \Sigma hkl \Sigma j |Ij - < Ij >| / \Sigma hkl \Sigma j |Ij|$, where hkl specifies unique indices, *j* indicates equivalent observations of *hkl*, and $< Ij >$ is the mean value.
[b] $R = \Sigma hkl ||F_o| - |F_c|| / \Sigma hkl |F_o|$, where $|F_o|$ and $|F_c|$ are the observed and calculated structure factor amplitudes, respectively.
[c] Represents approximately 10% of the data.

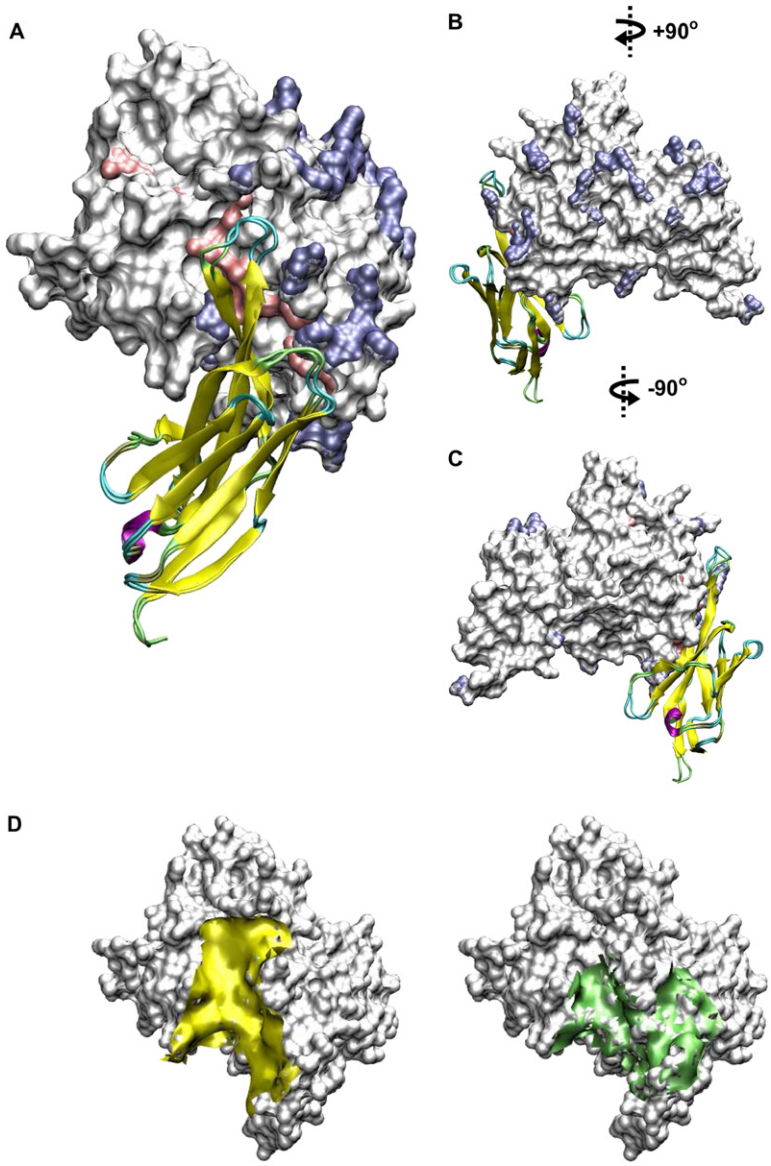

Figure 3. Structures of the AMA1-V_{NAR} Complexes

(A) Overlaid crystallographic complexes between V_{NAR} domains 14I-1 and 14I1-M15 (ribbons) and domains I and II of 3D7 AMA1 (surface representation). The elongated V_{NAR} CDR3 at the top of the molecule aligns with and penetrates the AMA1 surface-exposed hydrophobic cleft (pink). Polymorphic residues which contribute to malarial immune avoidance are shaded purple and represent highly variable epitope loops surrounding the conserved hydrophobic cleft.

(B) Alternative view of the complex. The polymorphic AMA1 face is only partially targeted by the V_{NAR} domains.

(C) Alternative view of the complex. The nonpolymorphic AMA1 face (putatively occluded on the parasite surface) is not targeted by the V_{NAR} domain.

(D) Comparison of AMA1 surface footprints for V_{NAR} 14I-1 (yellow) and murine antibody 1F9 Fab (PDB ID code: 2Q8A) (lime) domains. The distance threshold is 8 Å.

observed for two tyrosine residues within the CDR3 loop which reorient toward the center of the loop upon binding to lysozyme. The CDR1 loop in this case also underwent significant displacement upon antigen binding. We previously reported the effect of mutating residue 61 within this system (Kopsidas et al., 2006), which produced a clear enhancement in affinity. This residue is positioned at the apex of heavy loop 4 at the top of the V_{NAR} structure, ideally positioned to contact antigen. Surprisingly, in our structures, this residue does not interact with AMA1 and is positioned behind Lys32 and Asp33 (Lys61 Nz–Asp33 O = 3.4 Å). As V_{NAR} residue Asp33 potentially interacts with AMA1 Lys230 (3.5 Å), there is a possible functional role in supporting CDR1, although it is difficult to reconcile such long-range effects with a significant increase in affinity.

V_{NAR} Targeting of AMA1 Epitopes

The 14I-1 and 14I1-M15 V_{NAR}s contact a total of 21 and 22 residues, respectively (probe radius 4 Å), on the AMA1 molecule (Figure 5A; Table S3). Because of slight differences between the structures, potential hydrogen bond and salt bridge interactions vary for the two V_{NAR}s; a subset of these interactions is shown in Table 4. The majority of contacts are within the V_{NAR} CDR3 loops, with lesser but significant contributions from the CDR1 regions and residues Ala1-Trp2 at the N terminus of the V_{NAR} A strand (Figures 5B and 5C). The affinity-enhancing V_{NAR} mutation Arg92 identified in this study primarily contacts AMA1 residues Asn173, Gln174, and Pro185 in both structures (Table 4; Figures 6A and 6B), with additional contacts to Thr186 and Glu187 either below (14I-1) or above (14I1-M15) a 4 Å cutoff.

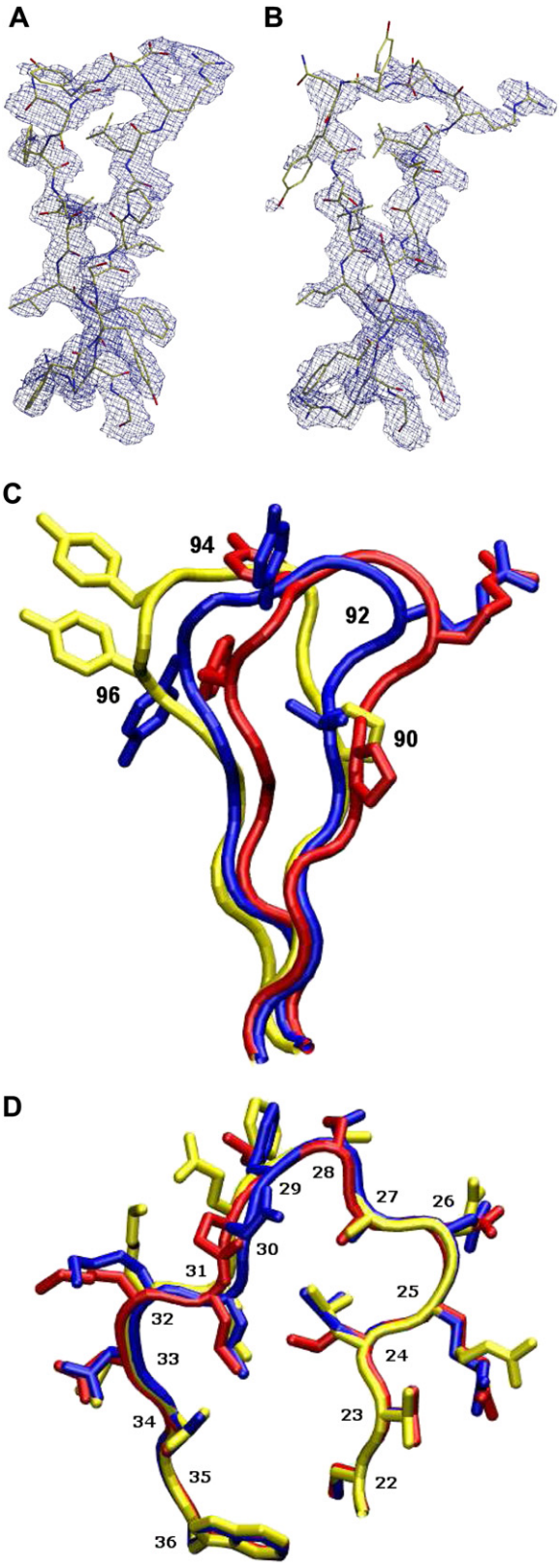

Figure 4. CDR Conformations upon AMA1 Binding

(A) Electron density $2F_o - F_c$ for the 14I-1 CDR3 loop (residues 86–102). The map is contoured at 1.0σ.

(B) Electron density $2F_o - F_c$ for the 14I1-M15 CDR3 loop (residues 86–102). The map is contoured at 1.0σ. Note the low level of visible density surrounding residues Tyr94 and Tyr96 at this contour.

(C) Superimposed representations of CDR3 backbone traces for V_{NAR}s 12Y-2 (yellow), 14I-1 (red), and 14I1-M15 (blue). Side chains are shown for residues Pro/Leu90, Arg92, Tyr94, and Tyr96.

(D) Superimposed representations of CDR1 backbone and side-chain traces for V_{NAR}s 12Y-2 (yellow), 14I-1 (red), and 14I1-M15 (blue).

The AMA1 hydrophobic cleft is formed by residues Val169, Leu176, Phe183, Met190, Tyr202, Val208, Met224, Tyr251, Ile252, Met273, Leu357, and Phe367. The V_{NAR} residues Tyr94 and Tyr96 potentially contact Tyr251 through aromatic ring interactions (5.3 Å) (Figure 6C; Table 4). This is a potentially important contact due to the extremely high conservation of Tyr251 in AMA1s across apicomplexan parasite species (Hehl et al., 2000). The structure of the 14I1-M15 loop appears slightly more flexible around Tyr96, allowing <4 Å contact with residue Asn228 compared to 14I-1 (>5.5 Å). An additional contact (5.3 Å) is present for 14I-1 through Asn371 and an associated water molecule (Figure 6C; Table 4). V_{NAR} residues Leu89 and Phe100 make close contact with the conserved hydrophobic cleft residues Met190, Tyr202, and Met224 (Figure 6D, shown in orange; Table 4) as part of a generalized series of salt bridge, hydrophobic, and aromatic interactions across the base and sides of the cleft. This additionally includes V_{NAR} residues Phe29/Leu29 inserting into a pocket formed by AMA1 residues Met190, Met193, Pro188, Phe201, and Tyr202. At the C terminus of the V_{NAR} CDR3 loop, residue Arg101 (range of contacts 2.7–3.4 Å) also makes significant charge and salt bridge contributions to binding, and there are additional possible contacts with residue Glu103 (Table 4).

To correlate levels of binding affinity and parasite inhibition with these structural data, we next mapped V_{NAR} residues that interact (<4 Å) with known AMA1 polymorphic residues (Figure 5A; Table S3). Significant polymorphisms (3D7-residue-W2mef/HB3) occur at positions Glu187Lys/Glu, Met190Met/Ile, Phe201Leu/Leu, and Ile225Asn/Asn. Most significant appear to be (1) Glu187Lys, where the change from negative to positive charge may affect the interaction with Arg92 on the CDR3 loop (Figure 6A); (2) Phe201Leu, where hydrophobic interactions within an aromatic pocket formed by V_{NAR} residues Phe29, Tyr87, and Phe100 of CDR3 and AMA1 residues Phe201 and Tyr202 may be disrupted (Figure 6D, cyan side chain); and (3) Ile225Asn, where mutation in W2mef and HB3 results in a change from hydrophobic to charged residue and may prejudice interactions with V_{NAR} Leu99 (3.0–3.8 Å) (Table 4). For HB3, in addition to the above residue changes, mutation Met190Ile (not present in W2mef) may affect the interaction with a hydrophobic pocket formed by V_{NAR} residues Leu89 and Phe100 (Figure 6D). Notwithstanding this dissection of interstrain differences, it should be noted that significantly more polymorphic variations than listed occur between these strains (Figure 5A). Although these are structurally removed by more than 4 Å from the V_{NAR} paratope, they are almost certain to exert long-range influence either by perturbing the conformation of the

hydrophobic cleft or by sterically altering orientation and access to the epitope by the antibody, sufficient to alter levels of binding affinity and parasite invasion inhibition within the observed one to two orders of magnitude.

DISCUSSION

By employing the protein-engineering techniques of targeted mutagenesis and library selection, we have expanded the binding tropism of a low-affinity shark IgNAR single-domain antibody fragment to AMA1 from three *Plasmodium* strains, and enhanced binding affinity by an order of magnitude. Even slight changes in CDR loop topology can lead to significant variations in antibody affinity, and the structures presented here illustrate this in the context of epitope binding by an unusually long CDR3 loop. Acquisition of just one dominant mutation (Gly92Arg) located at the apex of the CDR3 loop within the V_{NAR} paratope produced significant enhancement in potency, and we ascribe this effect to generation of a new series of hydrogen bond and salt bridge interactions with conserved AMA1 residues. However, the additive effects of other mutations also appeared necessary for enhanced biological potency, for example the Pro90Leu mutation resulting in potentially greater loop conformational freedom. Ultimately, because of the broad range of potential contacts within the 3–5 Å range encompassing an extensive network of V_{NAR}-AMA1 interactions, we are reluctant to definitively ascribe the differences between 14I-1 and 14I1-M15 to any single set of contacts.

The Kinetics versus Biological Activity Question for Antibody-Antigen Interactions

Of long-standing interest has been the mechanism by which protective antibodies directed against AMA1 inhibit red blood cell invasion, and how binding kinetics correlate with in vivo activity (Saul, 1987). Our data shed significant light on these issues by allowing us to compare the effect of defined mutations on both kinetic biosensor affinities and erythrocyte invasion inhibition. Within the constraints of comparing in vitro protein chemistry with a biological assay, it is interesting that the variants 14I-1 and 14I1-M15 both plateau at an affinity of ~5 nM, whereas 14I1-M15 was consistently more inhibitory of invasion. We suggest that the results from immobilization to a solid surface (Biacore) constrain AMA1 flexibility, compared to the greater inherent fluidity associated with presentation on the parasite surface. Additionally, the 14I1-M15 CDR loop appears more flexible in the crystallographic structures than its 14I-1 counterpart (as evidenced by electron density patterns), suggesting that increased conformational freedom leads to a superior fit upon antigen binding.

The measurable affinities of the antibody variants described here vary over an almost 400-fold range (above which binding is not detected), and the differences appear to be through prolonged dissociation phases (off-rates) rather than enhanced association (on-rates) for the complexes. Because of the overlapping standard errors for the results from multiple biosensor experiments, we are unable to conclusively answer the question of whether association rate is the true mediator of parasite invasion efficiency (Saul, 1987); however, our results strongly support a model where differences in the dissociation rate kinetics are at least equally as important in competition for the AMA1 ligand.

The Immune System: Parasite Arms Race and Implications for Anti-Malarial Drugs

Mechanistically, the multiple polymorphic loops surrounding the conserved hydrophobic cleft which bisects the AMA1 surface are ideally placed to foil molecules of the conventional vertebrate immune repertoire through a combination of steric hindrance and epitope variation. Thus, immunization of humans with AMA1 is unlikely to induce an antibody response that effectively targets the underlying conserved epitopes, as it requires a rare selection event in the host, as for the b12 anti-HIV gp120 antibody (Zhou et al., 2007), to produce this type of antibody paratope. However, our data, when combined with previous AMA1 structural studies, now illustrate the possibility of specific classes of single-domain reagents capable of penetrating and occupying the AMA1 cleft region. The success of camelid V_HH antibodies in targeting otherwise cryptic epitopes on variable surface glycoproteins of African trypanosomes (Stijlemans et al., 2004) is a similar and compelling example of parasite immune avoidance and counterstrategy by the vertebrate immune system, and suggests that such single-domain antibody structures may be particularly good at targeting parasite surfaces and similar antigenic sites that are refractory to antibody recognition (Colman et al., 1987).

Our future work will concentrate on structure-based mutagenesis and design of this family of V_{NAR} antibodies, aiming to target the more conserved AMA1 hydrophobic cleft residues and derive binding proteins capable of breaching the species barrier between *P. falciparum* and *P. vivax*. By extension to a murine model of malaria, we will be able to more fully correlate laboratory-based assays with efficacy in a living system. By understanding the mechanistic processes by which binding agents target this important malarial protein, we aim to guide our design of small-molecule drugs targeting this conserved region of AMA1 and thereby minimize the risk of evasion by the parasite, as well as advancing our understanding of the advantages offered by different forms of antibody architectures. Further, an understanding of the importance of individual AMA1 residues and the conformation they assume upon antibody binding will be equally applicable to the design of enhanced anti-AMA1 vaccines, where the influence of the polymorphic residues is ameliorated, while retaining the essence of the underlying neutralizing epitope.

EXPERIMENTAL PROCEDURES

Cloning and Construction of V_{NAR} Phage Display Library

Cell lines used for library propagation and protein expression were *E. coli* TG1 and *E. cloni* 10GF′ (Lucigen, Middleton, WI, USA). The

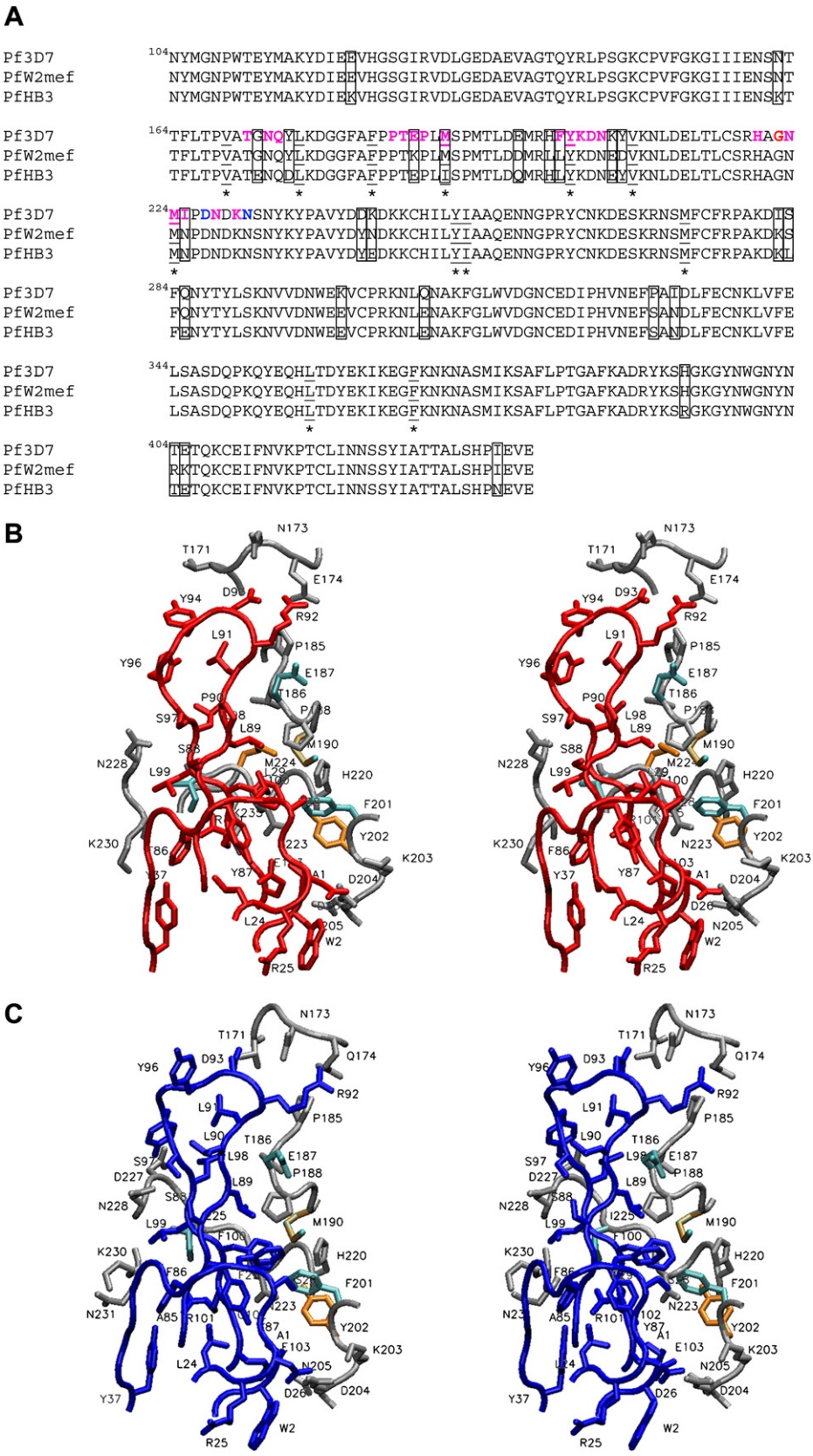
A
Pf3D7
PfW2mef
PfHB3
B
C
N173
T171
E174
Y94
D93
R92
L91
P185
Y96
E187
T186
P90
S97
L98
L89
P188
M190
S88
N228
L99
M224
H220
F201
K230
Y202
K203
Y87
D204
L24
N205
W2
R25

Table 4. Representative V_{NAR}-AMA1 Contacts

V_{NAR} AMA1/14I-1	Distance (Å)	V_{NAR} AMA1/14I1-M15	Distance (Å)
Leu89 CG–Thr186 CG2	3.8	Leu89 CA–Glu187 O	3.3
Leu89 CD1–Met190 CG	3.9	Leu89 CD2–Met190 CG	3.8
Arg92 NH2–Asn173 O	4.0	Arg92 NH1–Asn173 OD1	3.7
Arg92 NH2–Gln174 CG	3.3	Arg92 NH1–Glu174 CG	3.2
Arg92 N–Pro185 O	3.0	Arg92 N–Pro185 O	3.3
Arg92 N–Thr186 CA	3.9		
Arg92 CB–Glu187 CG	3.6		
Tyr94 OH–Thr171 O	3.6		
Tyr96 OH–Tyr251 OH	5.3	Tyr96 OH–Asn228 N	3.9
Leu98 CD2–Thr186 CD2	3.8		
Leu99 CB–Ile225 CB	3.5	Leu99 CB–Ile225 CB	3.8
Leu99 O–Ile225 N	3.0	Leu99 O–Ile225 N	3.4
Phe100 CA–Asn233 O	3.4	Phe100 CA–Asn233 O	3.6
Phe100 CD1–Met224 CE	3.3	Phe100 CD1–Met190 CG	3.7
Phe100 CZ–Phe201 CE2	3.5	Phe100 CZ–Asn233 CB	3.5
Phe100 CZ–Tyr202 OH	3.6	Phe100 CZ–Tyr202 OH	3.8
Arg101 N–Asn233 O	2.7	Arg101 N–Asn233 O	2.3
Arg101 NE–Gly222 O	2.9	Arg101 CZ–Ile225 CD1	4.0
Arg101 NH1–Gly222 O	3.4	Arg101 NH1–Lys230 O	3.1
Arg101 NH2–Ile225 CD1	3.0	Arg101 NH2–Ile225 CD1	3.0
Glu103 OE2–Asn205 ND2	3.0	Glu103 OE2–Asn205 ND2	2.4
Glu103 OE1–Asp204 O	3.9	Glu103 OE2–Asn205 CG	3.4

V_{NAR} library was constructed by splice-overlap PCR as previously described (Nuttall et al., 2003) using V_{NAR} 12Y-2-derived DNA templates (Nuttall et al., 2004). Loop randomization used six degenerate oligonucleotide primers (KH0001, KH0002, KH0003, KH0004, KH0005, KH0006; Table S1) and the 5′ primer 8408. Restriction endonuclease sites were added using oligonucleotide primer combination 8408 and 8404 (Table S1). Library cloning was as previously described (Nuttall et al., 2001) yielding a final library size of >5 × 10^7 clones. DNA sequencing (ABI Prism BigDye terminator cycle sequencing kit, v. 3.1, Applied Biosystems, Foster City, CA, USA; Australian Genome Research Facility, Melbourne) verified equal representation of randomization strategies in the final library.

AMA1 Protein Production

Variant recombinant *P. falciparum* AMA1 proteins from strains 3D7, W2mef, and HB3 were produced as described (Gupta et al., 2005; Hodder et al., 2001). In brief, proteins were expressed in *E. coli* with an N-terminal His tag, solubilized, purified using several nickel-NTA-affinity chromatography steps, and refolded in a buffer containing a redox couple. Proteins were further purified using anion-exchange chromatography, size-exclusion chromatography, and reverse-phase HPLC.

Selection of AMA1-Binding V_{NAR}s

Phagemid particles displaying the V_{NAR}-g3p fusion library were produced and biopanned (Nuttall et al., 2003) against AMA1 antigens (0.25–2.5 μg/ml) coated onto Maxisorb immunotubes (Nunc-Nalge International, Roskilde, Denmark). The wash regime was: round 1: 15 washes with PBS, 0.1% Tween 20; 15 washes with PBS; rounds 2, 3, and 4: 20 washes with PBS, 0.1% Tween 20; 20 washes with PBS. Post-fourth-round selection, eluted phages were infected into TG1 cells and propagated as plasmids (Nuttall et al., 2004).

Construction and Expression of V_{NAR} Variants

Seven V_{NAR} variants (Figure 1E) were constructed by sequential PCR using oligonucleotides 8408 (5′) and A1703, A1704, A1705, and 8404 (3′) (Table S1) in combination with V_{NAR} 12Y-2, 14M-8, and 14M-15 DNA templates (Nuttall et al., 2004). DNA cassettes were cloned as above and verified by bidirectional DNA sequencing. Recombinant V_{NAR} proteins were expressed into the *E. coli* periplasmic space

Figure 5. V_{NAR}-AMA1 Contacts

(A) Alignment of AMA1s from *P. falciparum* strains 3D7, W2mef, and HB3 (residues N104–E438). Residues polymorphic between strains are boxed. Conserved hydrophobic cleft residues are underlined and asterisked. Residues in contact with V_{NAR}s 14I-1 and 14I1-M15 (magenta), 14I-1 only (red), or 14I1-M15 only (blue) are indicated.

(B) Stereo images of the 14I-1 backbone (red) penetrating the AMA1 hydrophobic cleft (gray). Side chains of AMA1 residues within 4 Å of the V_{NAR} backbone are shown, including hydrophobic residues forming the base of the hydrophobic cleft (orange) and residues polymorphic between *P. falciparum* strains 3D7, W2mef, and HB3 (cyan).

(C) As for (B) except for 14I1-M15 backbone (blue).

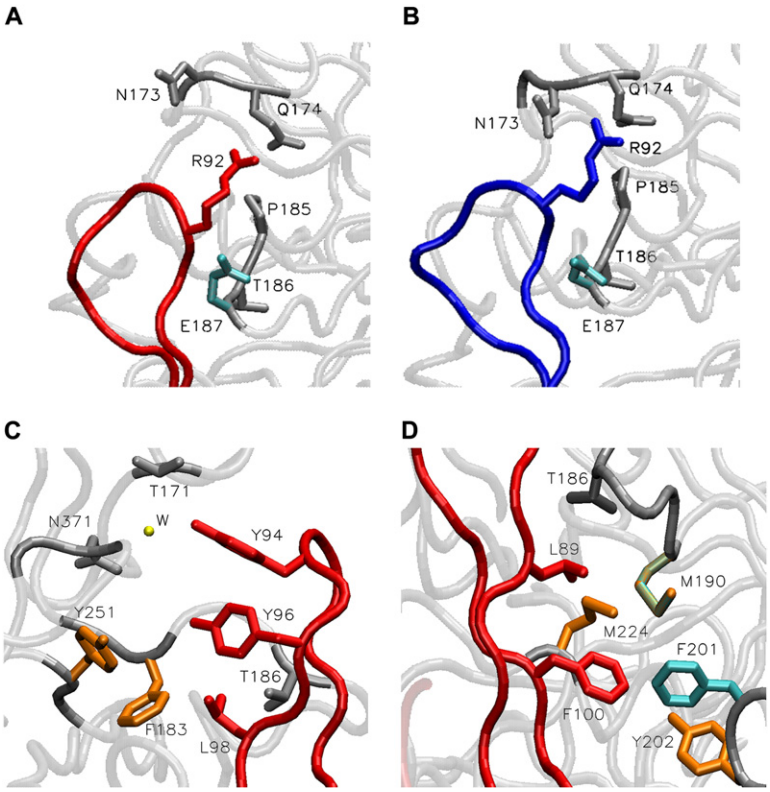

Figure 6. Mechanism of V_{NAR} Binding

(A) V_{NAR} residue Arg92 contacts AMA1 residues Asn173, Glu174, Pro185, Thr186, and Glu187 (<4 Å) in a series of hydrogen bond and salt bridge interactions in the 14I-1 crystallographic structure. Residue coloring is as for Figure 5.

(B) As for (A) except for the V_{NAR} 14I1-M15 structure.

(C) V_{NAR} residues Tyr94, Tyr96, and Leu98 in the 14I-1 structure contact hydrophobic cleft residues Phe183 and Tyr251, and associated residue Asn371, through a network of water-mediated hydrogen bonds and potential aromatic interactions.

(D) V_{NAR} residues Leu89 and Phe100 in the 14I-1 structure are closely associated with AMA1 residues within the hydropobic cleft (Met190, Tyr202, Met224) and residues polymorphic between *P. falciparum* strains (Met190, Phe201).

(Nuttall et al., 2001) and assayed in crude form, or purified by affinity chromatography through an anti-FLAG Ig/Sepharose column (10 × 1 cm) equilibrated in Tris-buffered saline. Proteins were analyzed by SDS-PAGE, western blotting, and size-exclusion chromatography (FPLC) on a precalibrated Superdex 75 column (Amersham Pharmacia Biotech, Uppsala, Sweden) in PBS (analytical) or 10 mM HEPES (pH 7.4), 150 mM NaCl, 0.05% Tween 20 (biosensor analysis). ELISA analysis was as described (Nuttall et al., 2004).

Determination of Binding Affinity by Surface Plasmon Resonance

A Biacore T100 biosensor (Papalia et al., 2006) was used to measure kinetic binding interactions between recombinant V_{NAR} and AMA1 proteins. All immobilizations were performed at 25°C with HBS-EP$^+$ buffer (10 mM HEPES [pH 7.4], 150 mM NaCl, 3.4 mM EDTA, 0.05% surfactant P20) as running buffer. AMA1 proteins were immobilized on CM5 sensor chips using standard amine-coupling chemistry: the carboxymethyl dextran surface was activated with 1:1 0.4 M 1-ethy-3-(3-dimethylaminopropyl) carbodiimide hydrochloride (EDC):0.1 M N-hydroxysuccinimide (NHS). "Aim-for-immobilized-level" wizard template (Biacore T100 control software; v. 1.1.1) was utilized for coupling of AMA1 proteins to the surface, whereby small volumes (1–9 μl) of AMA1 proteins (12.5 μg/ml, 10 mM sodium acetate [pH 4.5]) were automatically injected (5 μl/min) over the activated surface until immobilization of ~1000 RU was achieved. The immobilization procedure was completed by 1 M ethanolamine (pH 8.5) (7 min injection/10 μl/min) to deactivate residual reactive sites. All binding experiments were performed in HBS-EP$^+$ buffer at a constant flow rate (30 μl/min) with a series of analyte (V_{NAR}) concentrations. Regeneration of the AMA1 protein surface was achieved with a single 30 s injection of 10 mM glycine solution (pH 1.5). Binding data were evaluated using Scrubber software v.2.1 (http://www.biologic.com.au).

Parasite Culture and Invasion Inhibition Assays

P. falciparum strains were cultured as previously described (Lambros and Vanderberg, 1979) and synchronized using the sorbitol method (Trager and Jensen, 1976). Invasion inhibition assays were performed as described (Basco et al., 1995; Kennedy et al., 2002). Further details are available in the Supplemental Data.

Crystallization

Recombinant *P. falciparum* AMA1 domains I and II (Gupta et al., 2005) and V_{NAR}s 14I-1 or 14I1-M15 were mixed in 1:1 stoichiometric ratios and set up as 0.2 μl hanging drops (Cartesian honey bee 16 Robot; Genomic Solutions, Ann Arbor, MI, USA). Plates were incubated at 25°C. Successful conditions were scaled to 2 μl hanging drops. Final crystallization conditions for AMA1 DI and II and V_{NAR} 14I1-M15 were 0.1 M phosphate citrate (pH 4.2), 0.2 M NaCl, 20% polyethylene glycol (PEG) 8000. Diffraction-quality crystals (space group $P3_1$) were obtained after 48 hr. Final crystallization conditions for AMA1 DI and II and V_{NAR} 14I-1 were 0.1 M phosphate citrate (pH 4.2), 0.2 M NaCl, 15% PEG 8000. Diffraction-quality crystals (space group $P3_1$) were obtained after 48 hr.

Data Collection and Structure Determination

X-ray diffraction data were collected at the Photon Factory (Tsukuba, Japan). Data were collected at −160°C and processed using the HKL2000 suite (Otwinowski and Minor, 1997). Diffraction data statistics are summarized in Table 3. Location of the AMA1 and V_{NAR} domains was by molecular replacement using PHASER (McCoy et al., 2005). Search models were AMA1 (Bai et al., 2005) and V_{NAR} 12Y-1 (Streltsov et al., 2004). Phase improvement used BUSTER-TNT (Blanc et al., 2004) with the resultant electron density map used to build missing fragments. Model building and crystallographic refinement used iterative cycles of BUSTER-TNT and/or REFMAC5 (Murshudov et al., 1997) and manual model building using XtalView/Xfit (McRee, 1999).

Within BUSTER-TNT, scattering from missing atoms was modeled with a low-resolution homographic exponential distribution, and maximum entropy density completion was employed following each round of refinement to recover density for missing parts of the structure. Water molecules were added and revised with XtalView. Progress of the refinement was monitored using the R_{free} statistic based on a set encompassing 10% of the observed diffraction amplitudes. Following the convergence in standard REFMAC5 refinement, further improvement of R factors was achieved by refining all chains as separate rigid anisotropic domains with the translation, libration, and screw-rotation displacement procedure. The libration tensor showed significant anisotropy. The final refinement converged to R/R_{free} values of 0.201/0.284 and 0.189/0.282 for AMA1/14I-1 and AMA1/14I1-M15, respectively. Further details are given in the Supplemental Data.

Supplemental Data

The Supplemental Data include two figures, three tables, and Supplemental Experimental Procedures and can be found with this article online at http://www.structure.org/cgi/content/full/15/11/1452/DC1/.

ACKNOWLEDGMENTS

We thank the Photon Factory (Tsukuba, Japan) for access to beamline 17A; Dr. Karen Harris for advice on AMA1 binding assays; Ms. Megan Hattarki for assistance with surface plasmon resonance measurements; Ms. Pat Pilling for assistance with protein crystallization procedures; and Ms. Ronelle Welton for assistance with protein expression. This work was supported by the Australian Synchrotron Research Program, which is funded by the Commonwealth of Australia under the Major National Research Facilities Program, and by the National Institutes of Health (RO1AI59229).

Received: July 8, 2007
Revised: August 13, 2007
Accepted: September 10, 2007
Published: November 13, 2007

REFERENCES

Alexander, D.L., Arastu-Kapur, S., Dubremetz, J.F., and Boothroyd, J.C. (2006). *Plasmodium falciparum* AMA1 binds a rhoptry neck protein homologous to TgRON4, a component of the moving junction in *Toxoplasma gondii*. Eukaryot. Cell *5*, 1169–1173.

Bai, T., Becker, M., Gupta, A., Strike, P., Murphy, V.J., Anders, R.F., and Batchelor, A.H. (2005). Structure of AMA1 from *Plasmodium falciparum* reveals a clustering of polymorphisms that surround a conserved hydrophobic pocket. Proc. Natl. Acad. Sci. USA *102*, 12736–12741.

Basco, L.K., Marquet, F., Makler, M.M., and Le Bras, J. (1995). *Plasmodium falciparum* and *Plasmodium vivax*: lactate dehydrogenase activity and its application for in vitro drug susceptibility assay. Exp. Parasitol. *80*, 260–271.

Blanc, E., Roversi, P., Vonrhein, C., Flensburg, C., Lea, S.M., and Bricogne, G. (2004). Refinement of severely incomplete structures with maximum likelihood in BUSTER-TNT. Acta Crystallogr. D Biol. Crystallogr. *60*, 2210–2221.

Cheng, Q., and Saul, A. (1994). Sequence analysis of the apical membrane antigen I (AMA-1) of *Plasmodium vivax*. Mol. Biochem. Parasitol. *65*, 183–187.

Coley, A.M., Parisi, K., Masciantonio, R., Hoeck, J., Casey, J.L., Murphy, V.J., Harris, K.S., Batchelor, A.H., Anders, R.F., and Foley, M. (2006). The most polymorphic residue on *Plasmodium falciparum* apical membrane antigen 1 determines binding of an invasion-inhibitory antibody. Infect. Immun. *74*, 2628–2636.

Coley, A.M., Gupta, A., Murphy, V.J., Bai, T., Kim, H., Anders, R.F., Foley, M., and Batchelor, A.H. (2007). Structure of the malaria antigen AMA1 in complex with a growth-inhibitory antibody. PLoS Pathog. *3*, 1308–1319.

Collis, A.V., Brouwer, A.P., and Martin, A.C. (2003). Analysis of the antigen combining site: correlations between length and sequence composition of the hypervariable loops and the nature of the antigen. J. Mol. Biol. *325*, 337–354.

Colman, P.M., Air, G.M., Webster, R.G., Varghese, J.N., Baker, A.T., Lentz, M.R., Tulloch, P.A., and Laver, W.G. (1987). How antibodies recognise virus proteins. Immunol. Today *8*, 323–326.

Cortes, A., Mellombo, M., Mueller, I., Benet, A., Reeder, J.C., and Anders, R.F. (2003). Geographical structure of diversity and differences between symptomatic and asymptomatic infections for *Plasmodium falciparum* vaccine candidate AMA1. Infect. Immun. *71*, 1416–1426.

De Genst, E., Silence, K., Decanniere, K., Conrath, K., Loris, R., Kinne, J., Muyldermans, S., and Wyns, L. (2006). Molecular basis for the preferential cleft recognition by dromedary heavy-chain antibodies. Proc. Natl. Acad. Sci. USA *103*, 4586–4591.

Dooley, H., Flajnik, M.F., and Porter, A.J. (2003). Selection and characterization of naturally occurring single-domain (IgNAR) antibody fragments from immunized sharks by phage display. Mol. Immunol. *40*, 25–33.

Dutta, S., Haynes, J.D., Barbosa, A., Ware, L.A., Snavely, J.D., Moch, J.K., Thomas, A.W., and Lanar, D.E. (2005). Mode of action of invasion-inhibitory antibodies directed against apical membrane antigen 1 of *Plasmodium falciparum*. Infect. Immun. *73*, 2116–2122.

Greenberg, A.S., Steiner, L., Kasahara, M., and Flajnik, M.F. (1993). Isolation of a shark immunoglobulin light chain cDNA clone encoding a protein resembling mammalian κ light chains: implications for the evolution of light chains. Proc. Natl. Acad. Sci. USA *90*, 10603–10607.

Gupta, A., Bai, T., Murphy, V., Strike, P., Anders, R.F., and Batchelor, A.H. (2005). Refolding, purification, and crystallization of apical membrane antigen 1 from *Plasmodium falciparum*. Protein Expr. Purif. *41*, 186–198.

Hamers-Casterman, C., Atarhouch, T., Muyldermans, S., Robinson, G., Hamers, C., Songa, E.B., Bendahman, N., and Hamers, R. (1993). Naturally occurring antibodies devoid of light chains. Nature *363*, 446–448.

Healer, J., Crawford, S., Ralph, S., McFadden, G., and Cowman, A.F. (2002). Independent translocation of two micronemal proteins in developing *Plasmodium falciparum* merozoites. Infect. Immun. *70*, 5751–5758.

Hehl, A.B., Lekutis, C., Grigg, M.E., Bradley, P.J., Dubremetz, J.F., Ortega-Barria, E., and Boothroyd, J.C. (2000). *Toxoplasma gondii* homologue of *Plasmodium* apical membrane antigen 1 is involved in invasion of host cells. Infect. Immun. *68*, 7078–7086.

Hodder, A.N., Crewther, P.E., and Anders, R.F. (2001). Specificity of the protective antibody response to apical membrane antigen 1. Infect. Immun. *69*, 3286–3294.

Holliger, P., and Hudson, P.J. (2005). Engineered antibody fragments and the rise of single domains. Nat. Biotechnol. *23*, 1126–1136.

Kennedy, M.C., Wang, J., Zhang, Y., Miles, A.P., Chitsaz, F., Saul, A., Long, C.A., Miller, L.H., and Stowers, A.W. (2002). In vitro studies with recombinant *Plasmodium falciparum* apical membrane antigen 1 (AMA1): production and activity of an AMA1 vaccine and generation of a multiallelic response. Infect. Immun. *70*, 6948–6960.

Kopsidas, G., Roberts, A.S., Coia, G., Streltsov, V.A., and Nuttall, S.D. (2006). In vitro improvement of a shark IgNAR antibody by Qβ replicase mutation and ribosome display mimics in vivo affinity maturation. Immunol. Lett. *107*, 163–168.

Kwong, P.D., Doyle, M.L., Casper, D.J., Cicala, C., Leavitt, S.A., Majeed, S., Steenbeke, T.D., Venturi, M., Chaiken, I., Fung, M., et al. (2002). HIV-1 evades antibody-mediated neutralization through conformational masking of receptor-binding sites. Nature *420*, 678–682.

Lambros, C., and Vanderberg, J.P. (1979). Synchronization of *Plasmodium falciparum* erythrocytic stages in culture. J. Parasitol. *65*, 418–420.

Lawrence, M.C., and Colman, P.M. (1993). Shape complementarity at protein/protein interfaces. J. Mol. Biol. *234*, 946–950.

Liu, J.L., Anderson, G.P., Delehanty, J.B., Baumann, R., Hayhurst, A., and Goldman, E.R. (2007). Selection of cholera toxin specific IgNAR single-domain antibodies from a naive shark library. Mol. Immunol. *44*, 1775–1783.

Marshall, V.M., Zhang, L., Anders, R.F., and Coppel, R.L. (1996). Diversity of the vaccine candidate AMA-1 of *Plasmodium falciparum*. Mol. Biochem. Parasitol. *77*, 109–113.

McCoy, A.J., Grosse-Kunstleve, R.W., Storoni, L.C., and Read, R.J. (2005). Likelihood-enhanced fast translation functions. Acta Crystallogr. D Biol. Crystallogr. *61*, 458–464.

McRee, D.E. (1999). XtalView/Xfit—a versatile program for manipulating atomic coordinates and electron density. J. Struct. Biol. *125*, 156–165.

Murshudov, G.N., Vagin, A.A., and Dodson, E.J. (1997). Refinement of macromolecular structures by the maximum-likelihood method. Acta Crystallogr. D Biol. Crystallogr. *53*, 240–255.

Narum, D.L., and Thomas, A.W. (1994). Differential localization of full-length and processed forms of PF83/AMA-1 an apical membrane antigen of *Plasmodium falciparum* merozoites. Mol. Biochem. Parasitol. *67*, 59–68.

Nguyen, V.K., Su, C., Muyldermans, S., and van der Loo, W. (2002). Heavy-chain antibodies in *Camelidae*; a case of evolutionary innovation. Immunogenetics *54*, 39–47.

Nuttall, S.D., Irving, R.A., and Hudson, P.J. (2000). Immunoglobulin VH domains and beyond: design and selection of single-domain binding and targeting reagents. Curr. Pharm. Biotechnol. *1*, 253–263.

Nuttall, S.D., Krishnan, U.V., Hattarki, M., De Gori, R., Irving, R.A., and Hudson, P.J. (2001). Isolation of the new antigen receptor from wobbegong sharks, and use as a scaffold for the display of protein loop libraries. Mol. Immunol. *38*, 313–326.

Nuttall, S.D., Krishnan, U.V., Doughty, L., Pearson, K., Ryan, M.T., Hoogenraad, N.J., Hattarki, M., Carmichael, J.A., Irving, R.A., and Hudson, P.J. (2003). Isolation and characterization of an IgNAR variable domain specific for the human mitochondrial translocase receptor Tom70. Eur. J. Biochem. *270*, 3543–3554.

Nuttall, S.D., Humberstone, K.S., Krishnan, U.V., Carmichael, J.A., Doughty, L., Hattarki, M., Coley, A.M., Casey, J.L., Anders, R.F., Foley, M., et al. (2004). Selection and affinity maturation of IgNAR variable domains targeting *Plasmodium falciparum* AMA1. Proteins *55*, 187–197.

Otwinowski, Z., and Minor, W. (1997). Processing of X-ray diffraction data collected in oscillation mode. In Methods in Enzymology, C.W. Carter, Jr. and R.M. Sweet, eds. (New York: Academic Press), pp. 307–326.

Papalia, G.A., Baer, M., Luehrsen, K., Nordin, H., Flynn, P., and Myszka, D.G. (2006). High-resolution characterization of antibody fragment/antigen interactions using Biacore T100. Anal. Biochem. *359*, 112–119.

Peterson, M.G., Marshall, V.M., Smythe, J.A., Crewther, P.E., Lew, A., Silva, A., Anders, R.F., and Kemp, D.J. (1989). Integral membrane protein located in the apical complex of *Plasmodium falciparum*. Mol. Cell. Biol. *9*, 3151–3154.

Pizarro, J.C., Vulliez-Le Normand, B., Chesne-Seck, M.L., Collins, C.R., Withers-Martinez, C., Hackett, F., Blackman, M.J., Faber, B.W., Remarque, E.J., Kocken, C.H., et al. (2005). Crystal structure of the malaria vaccine candidate apical membrane antigen 1. Science *308*, 408–411.

Polley, S.D., Chokejindachai, W., and Conway, D.J. (2003). Allele frequency-based analyses robustly map sequence sites under balancing selection in a malaria vaccine candidate antigen. Genetics *165*, 555–561.

Roux, K.H., Greenberg, A.S., Greene, L., Strelets, L., Avila, D., McKinney, E.C., and Flajnik, M.F. (1998). Structural analysis of the nurse shark (new) antigen receptor (NAR): molecular convergence of NAR and unusual mammalian immunoglobulins. Proc. Natl. Acad. Sci. USA *95*, 11804–11809.

Saul, A. (1987). Kinetic constraints on the development of a malaria vaccine. Parasite Immunol. *9*, 1–9.

Simmons, D.P., Streltsov, V.A., Dolezal, O., Hudson, P.J., Coley, A.M., Foley, M., Proll, D.F., and Nuttall, S.D. (2007). Shark IgNAR antibody mimotopes target a murine immunoglobulin through extended CDR3 loop structures. Proteins, in press.

Stanfield, R.L., Dooley, H., Flajnik, M.F., and Wilson, I.A. (2004). Crystal structure of a shark single-domain antibody V region in complex with lysozyme. Science *305*, 1770–1773.

Stanfield, R.L., Dooley, H., Verdino, P., Flajnik, M.F., and Wilson, I.A. (2007). Maturation of shark single-domain (IgNAR) antibodies: evidence for induced-fit binding. J. Mol. Biol. *367*, 358–372.

Stijlemans, B., Conrath, K., Cortez-Retamozo, V., Van Xong, H., Wyns, L., Senter, P., Revets, H., De Baetselier, P., Muyldermans, S., and Magez, S. (2004). Efficient targeting of conserved cryptic epitopes of infectious agents by single domain antibodies. African trypanosomes as paradigm. J. Biol. Chem. *279*, 1256–1261.

Streltsov, V., and Nuttall, S. (2005). Do sharks have a new antibody lineage? Immunol. Lett. *97*, 159–160.

Streltsov, V.A., Varghese, J.N., Carmichael, J.A., Irving, R.A., Hudson, P.J., and Nuttall, S.D. (2004). Structural evidence for evolution of shark Ig new antigen receptor variable domain antibodies from a cell-surface receptor. Proc. Natl. Acad. Sci. USA *101*, 12444–12449.

Trager, W., and Jensen, J.B. (1976). Human malaria parasites in continuous culture. Science *193*, 673–675.

Varghese, J.N. (1999). Development of neuraminidase inhibitors as anti-influenza virus drugs. Drug Dev. Res. *46*, 176–196.

Varghese, J.N., Smith, P.W., Sollis, S.L., Blick, T.J., Sahasrabudhe, A., McKimm-Breschkin, J.L., and Colman, P.M. (1998). Drug design against a shifting target: a structural basis for resistance to inhibitors in a variant of influenza virus neuraminidase. Structure *6*, 735–746.

WHO/UNICEF. (2005). World Malaria Report (http://rbm.who.int/wmr2005/).

Zhou, J., Zhang, G., Nishikawa, Y., Fujisaki, K., and Xuan, X. (2006). A 38-kDa protein from *Babesia gibsoni* and its antibody response in an experimentally infected dog. Vet. Parasitol. *141*, 345–348.

Zhou, T., Xu, L., Dey, B., Hessell, A.J., Van Ryk, D., Xiang, S.H., Yang, X., Zhang, M.Y., Zwick, M.B., Arthos, J., et al. (2007). Structural definition of a conserved neutralization epitope on HIV-1 gp120. Nature *445*, 732–737.

Accession Numbers

The Protein Data Bank ID codes for the crystal structures are 2Z8V (AMA1/14I-1) and 2Z8W (AMA1/14I1-M15).

